catalysts

MDPI

Article

$FeCeO_x$ Supported Ni, Sn Catalysts for the High-Temperature Water–Gas Shift Reaction

Devaiah Damma * and Panagiotis G. Smirniotis *

Chemical Engineering, College of Engineering and Applied Science, University of Cincinnati, Cincinnati, OH 45221-0012, USA

* Correspondence: dammadh@ucmail.uc.edu (D.D.); smirnipp@ucmail.uc.edu (P.G.S.); Tel.: +1-513-556-1474 (P.G.S.); Fax: +1-513-556-3473 (P.G.S.)

Received: 11 May 2020; Accepted: 6 June 2020; Published: 8 June 2020

Abstract: In this work, the effect of monometallic Ni or Sn and bimetallic NiSn deposition on the activity of $FeCeO_x$ catalysts in high-temperature water–gas (HT-WGS) reactions was investigated. It was found that the HT-WGS performance of $FeCeO_x$ has significantly improved after the deposition of Sn together with Ni on it. Furthermore, the bimetallic NiSn/$FeCeO_x$ catalyst showed higher activity compared to the monometallic Ni/$FeCeO_x$ and Sn/$FeCeO_x$ catalysts within the tested temperature range (450–600 °C). Although the Ni/$FeCeO_x$ catalyst showed methanation activity at a temperature below 550 °C, the NiSn/$FeCeO_x$ catalyst suppressed the methane formation to zero in the WGS. Besides, the NiSn/$FeCeO_x$ catalyst exhibited an excellent time-on-stream stability without methanation reaction, even at a steam-to-CO ratio as low as 0.8. The combination of Ni and Sn supported on $FeCeO_x$ led to a large lattice strain, the formation of NiSn alloy, and a strong synergistic effect between the bimetallic NiSn and $FeCeO_x$ mixed oxide support interface. All these features are very important in achieving the best activity and stability of NiSn/$FeCeO_x$ in the HT-WGS reaction.

Keywords: high-temperature water–gas shift; Ni-based catalysts; NiSn bimetallic catalysts; methane suppression

1. Introduction

The efforts to produce hydrogen energy are an ongoing important research topic as hydrogen is a clean, renewable, and highly efficient energy carrier that can effectively solve the problem of energy shortage and environmental pollution [1,2]. A water–gas shift (WGS) reaction is a widely employed process to efficiently produce hydrogen for many modern technological applications. In particular, the high-temperature water–gas shift (HT-WGS) reaction has received renewed attention in relation to the production of hydrogen through the gasification of coal, agricultural/forestry biomass, and municipal wastes [3]. Industrially, Fe–Cr-based spinels had been proven to be a promising catalyst for HT-WGS in the temperature range of 350–450 °C. However, the hexavalent chromium found in iron–chromium mixed oxide catalyst during the WGS reaction could threaten human life and the environment due to its potent carcinogenic nature [4–6]. Moreover, an excess steam ($H_2O/CO \approx 5$) is used in the industry to maintain the catalyst stability by preventing over-reduction of the catalyst by CO stream. However, the CO-rich gas stream is usually emitted from the gasification process at high temperatures (above 450 °C), which leads to the catalyst deactivation [7]. Hence, the commercial catalyst could not be suitable for the WGS reaction under the conditions of gasification process. It is of great interest to develop highly active and stable Cr-free catalysts for HT-WGS reactions.

Recently, supported Ni-based catalysts have received tremendous attention for HT-WGS because of their high CO conversion and low price [8]. However, supported monometallic Ni-based catalysts show high activity toward undesired methanation reactions, which consume hydrogen and consequently reduces

the selectivity toward the WGS reaction [9]. Few attempts have been made to circumvent the methane formation by introducing a second metal promoter to supported Ni-based catalysts. Especially, Cu is the widely reported secondary metal to Ni-based catalysts for the inhibition of methane in WGS [3,9–11]. For example, CeO_2 supported bimetallic Ni–Cu catalysts have been shown to exhibit superior activity and selectivity by suppressing methane formation in the HT-WGS. The Ni–Cu alloy phase that formed during the pre-reduction was reported to play a critical role in suppressing the methanation reaction because Ni–Cu alloy can enhance CO adsorption which prevents CO dissociation during HT-WGS reaction [10,11]. Apart from traditional Cu as a secondary promoter, other metals such as Fe or Re have also been used to form Ni-based bimetallic catalyst formulations [12,13]. However, the methanation activity of Re-Ni based bimetallic catalysts in WGS has not been reported [12]. On the other hand, the Ni–Fe-based catalysts have been studied in the low-temperature region (≤450 °C), which showed CO methanation reaction [13]. Typically, the hydrogenation of CO/CO_2 produces undesirable methane during the WGS. It has been reported that the hydrogenation activity of Ni-based catalysts is inhibited by the addition of Sn due to the formation of an NiSn intermetallic structure [14,15]. The suppression of the methane formation has also recently been observed with the NiSn/(In)ZrO_2 system in the CO_2 hydrogenation reaction. The combination of a Ni and Sn catalyst was found to significantly decrease the rate of methane formation by increasing the rate of methanol production as compared to the monometallic Ni catalyst [16]. The addition of a Sn promoter to Ni has also remarkably increased the selectivity toward the formation of hydrogen from biomass-derived hydrocarbons as compared to the monometallic Ni, which predominantly showed enhanced selectivity toward the production of alkanes [17]. In spite of these interesting results, as far as we know, a study that uses bimetallic NiSn-based material as a catalyst for WGS has not been previously reported.

Although Ni-based bimetallic nanostructures are commonly claimed to be the main component of the active site for WGS, the support material has also been shown to play a significant role in suppressing the methane formation. For instance, Wang et al. [18] have compared the role of various oxide supports on WGS performance of PtNi bimetallic catalyst and found that the suppression of methane followed the order of PtNi/SiO_2 < PtNi/CeO_2 ~ PtNi/γ-Al_2O_3 < PtNi/TiO_2 ~ PtNi/high surface area–ZrO_2. Jha et al. [3] unveiled that the Fe_2O_3-supported catalysts effectively minimize the methane formation in the WGS reaction compared to CeO_2-supported catalysts. However, Fe_2O_3-supported catalysts had lower CO conversion than that of CeO_2-supported catalysts. Thus, the choice of support is also crucial to obtain high activity and selectivity in WGS. Our previous work demonstrated that if a suitable amount of Ce cations was doped into the matrix of iron oxide, it resulted in a highly active HT-WGS catalyst without methanation [19]. From this finding, it is thus expected that the Fe–Ce mixed oxide could be promising support for bimetallic NiSn catalysts to achieve better HT-WGS performance. However, to the best of our knowledge, no work can be found using Fe–Ce composite oxide as support for Ni, Sn metals to develop an improved catalyst for WGS reaction.

In this work, the effect of monometallic Ni or Sn and bimetallic NiSn loading on the HT-WGS performance of $FeCeO_x$ was investigated. The deposition of bimetallic NiSn has significantly enhanced the HT-WGS activity of $FeCeO_x$ in comparison to the monometallic Ni/$FeCeO_x$ and Sn/$FeCeO_x$ catalysts. In addition, the NiSn/$FeCeO_x$ catalyst maintains a stable performance for 50 h without methanation reaction even under low steam to CO ratio of 0.8. H_2-TPR and XPS results showed the formation of NiSn alloy over the surface of the NiSn/$FeCeO_x$ catalyst, which plays a key role in improving the activity and stability by suppressing the methane formation in HT-WGS reaction.

2. Results and Discussion

2.1. Catalytic Activity, Selectivity, and Stability

The WGS performance of the catalysts was tested at a steam-to-CO ratio of 1.5 and a temperature range of 450 to 600 °C. The fresh catalysts were firstly reduced in situ at 400 °C for 2 h in process gas to conduct the WGS reaction. The temperature-dependent CO conversion in WGS over $FeCeO_x$, Ni/$FeCeO_x$,

$Sn/FeCeO_x$, and $NiSn/FeCeO_x$ catalysts are displayed in Figure 1a. As can be seen, $FeCeO_x$ gives the CO conversion of 50.9–65.9% within the tested temperature range. Below 550 °C, the deposition of Ni on the $FeCeO_x$ has enhanced the CO conversion compared to the $FeCeO_x$ sample. This suggests the promotional effect of Ni on the WGS performance of $FeCeO_x$ at lower temperature. The improved WGS activity of $Ni/FeCeO_x$ could be attributed to the high CO conversion rate of Ni in the catalyst [10,20]. However, the monometallic $Ni/FeCeO_x$ exhibited lower CO conversion than the $FeCeO_x$ at temperature of above 550 °C. On the other hand, the CO conversion was decreased after the loading of Sn over the $FeCeO_x$ at below 550 °C. This indicates the poor promotional effect of Sn than Ni on the WGS activity of $FeCeO_x$ catalyst at temperature lower than 550 °C. Surprisingly, the monometallic $Sn/FeCeO_x$ catalyst showed higher WGS performance as compared to the $FeCeO_x$ sample at above 550 °C. This suggests the pronounced activity promotion at higher temperature by Sn introduction into the $FeCeO_x$. It is noteworthy that the monometallic $Sn/FeCeO_x$ catalyst achieved a CO conversion of 70.6% at 600 °C, which is close to that of the theoretical equilibrium level of CO conversion of 72.9%. Interestingly, the combination Ni and Sn supported on $FeCeO_x$ significantly increased the CO conversion in WGS. The CO conversion of bimetallic $NiSn/FeCeO_x$ catalyst reached the equilibrium level in the temperature range of 550–600 °C. Moreover, the catalytic performance of bimetallic $NiSn/FeCeO_x$ is higher than that of both the monometallic $Ni/FeCeO_x$ and $Sn/FeCeO_x$ catalysts over the investigated temperature range. These results imply that both the Ni and Sn greatly promote the WGS in the bimetallic $NiSn/FeCeO_x$ catalyst than in the monometallic $Ni/FeCeO_x$ and $Sn/FeCeO_x$ samples.

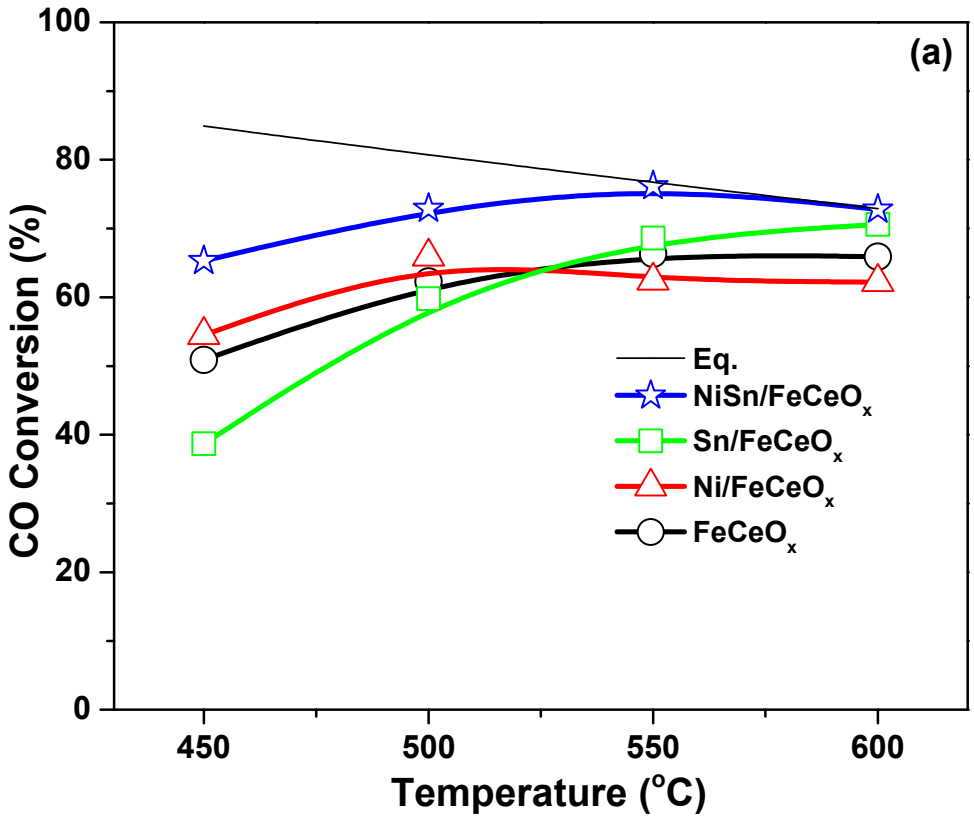

Figure 1. *Cont.*

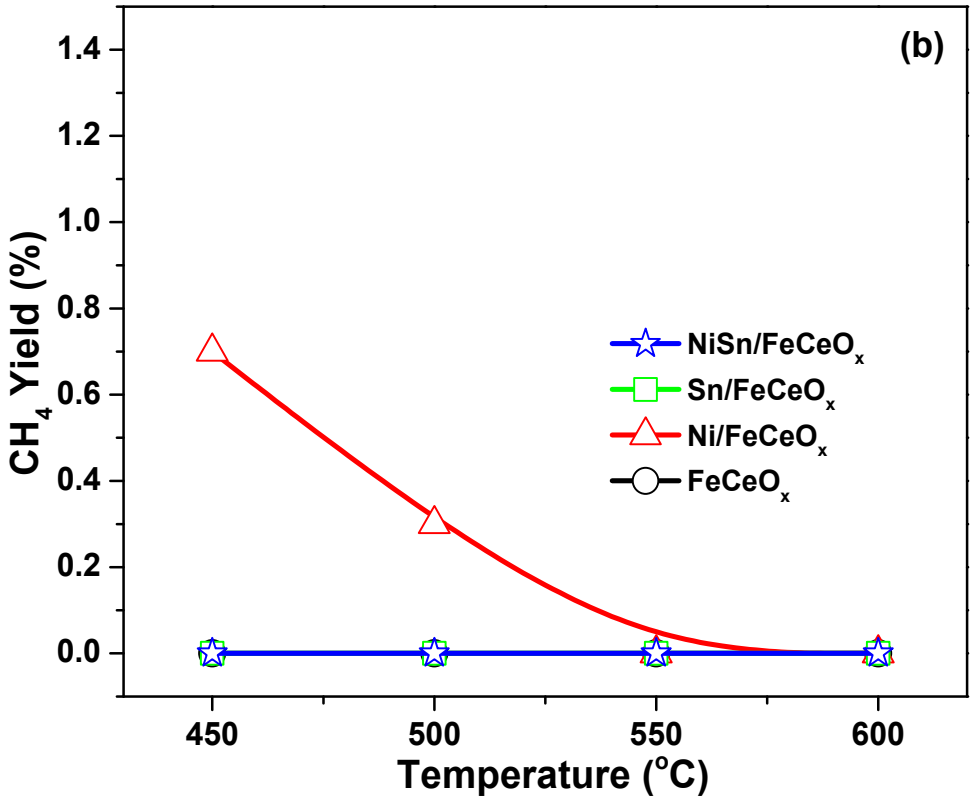

Figure 1. (**a**) High-temperature water–gas shift (HT-WGS) activity and (**b**) methane yield (%) over the $FeCeO_x$, $Ni/FeCeO_x$, $Sn/FeCeO_x$, and $NiSn/FeCeO_x$ catalysts at a steam-to-CO ratio of 1.5.

It is widely reported that the Ni-based catalysts are highly active for undesirable CO methanation reaction in WGS [3,9,10,20]. Thus, it is also important to know the selectivity in WGS as methanation consumes 3 moles of hydrogen, which significantly decreases the hydrogen yield [21]. The methane yield over all the catalysts is depicted in Figure 1b. No methane formation was observed over the $FeCeO_x$ catalyst. The deposition of Ni on the $FeCeO_x$ resulted in the formation of methane (0.3–0.7% yield) at temperature below 550 °C. At above 550 °C, the methanation activity of monometallic $Ni/FeCeO_x$ catalysts abruptly decreases to zero. This indicates that the higher CO conversion of monometallic $Ni/FeCeO_x$ as compared to the $FeCeO_x$ at temperature below 550 °C is accompanied by methanation reaction. However, the addition of Sn to the $FeCeO_x$ did not favor the methane formation in the range of tested temperature. Interestingly, although monometallic $Ni/FeCeO_x$ showed the methane formation, the loading of Ni together with Sn over $FeCeO_x$ support has suppressed the methanation activity to zero in the whole investigated temperature region. This could be due to the synergistic interaction between the Ni and Sn in the catalyst.

The long-term stability of bimetallic $NiSn/FeCeO_x$ was also investigated at 500 °C and steam to CO ratio of 1.5 for 50 h. As can be observed from Figure 2a, the $NiSn/FeCeO_x$ exhibited stable CO conversion without any methanation throughout the 50 h runtime. To better understand the performance of the catalyst in terms of methane suppression, the steam-to-CO ratio has been reduced to 0.8 from 1.5 as a low steam-to-CO ratio favors the methane formation. Surprisingly, the catalyst showed stable performance (Figure 2a) and suppressed the methane formation even under a low steam-to-CO ratio of 0.8 (Figure 2b). These findings suggest that the deposition of Ni and Sn together on $FeCeO_x$ offered an excellent time on stream stability without methanation reaction during HT-WGS.

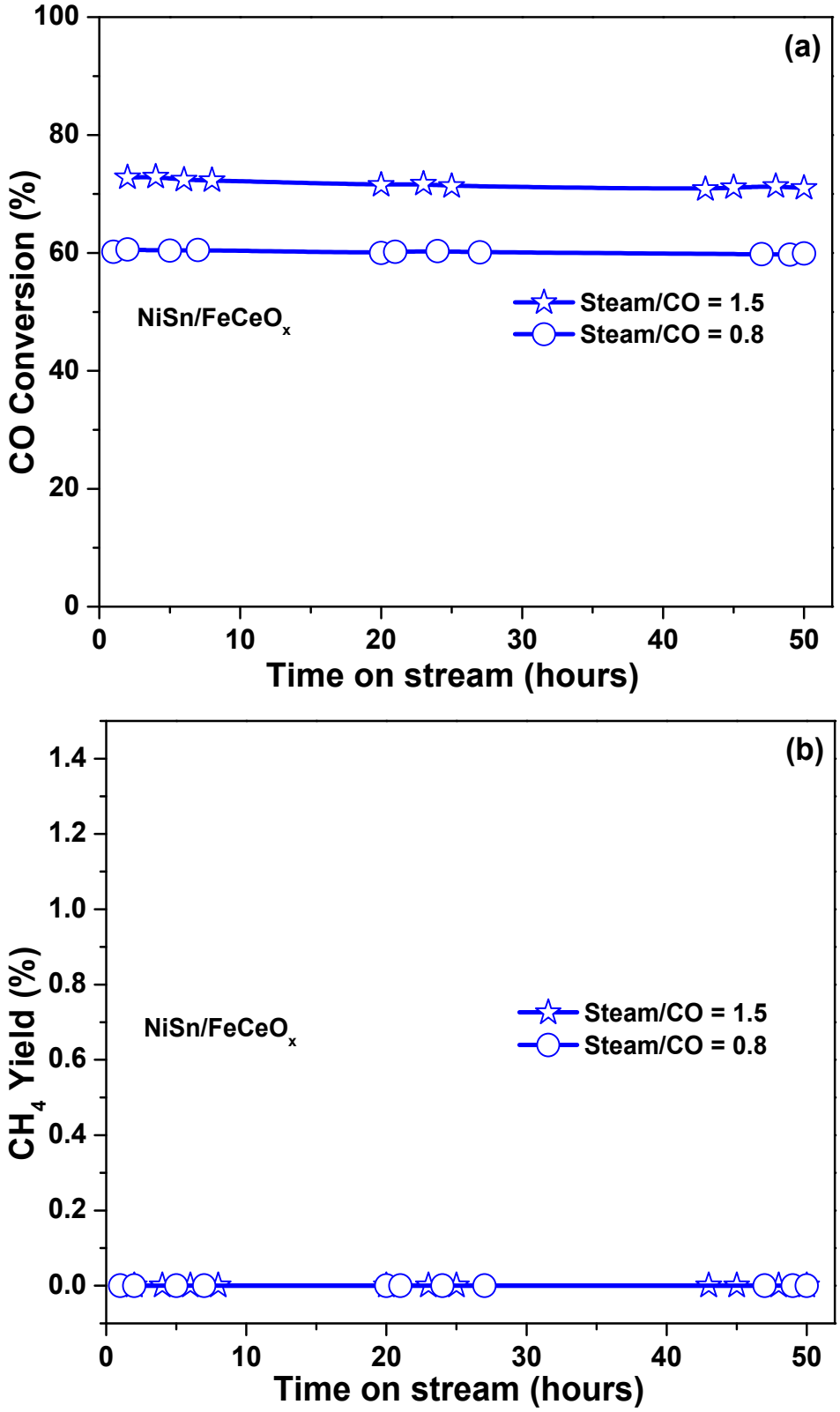

Figure 2. (**a**) CO conversion (%); (**b**) methane yield (%) with time on stream over the NiSn/FeCeO$_x$ catalyst (steam/CO = 1.5 and 0.8, T = 500 °C).

2.2. Catalyst Characterization

2.2.1. X-ray Diffraction (XRD) Measurement

XRD patterns of the fresh (calcined) $FeCeO_x$ and $FeCeO_x$ supported monometallic Ni, Sn, and bimetallic NiSn catalysts are shown in Figure 3a. All of the samples showed the diffraction peaks corresponding to the hematite (Fe_2O_3) phase (JCPDS 33-0664) of iron oxide. In addition, two reflections at around 28.7° and 47.6° were found in all the samples, which can be attributed to the (111) and (220) planes of the CeO_2 phase (JCPDS 34-0394), respectively [22,23]. However, no diffraction patterns corresponding to the Ni and Sn oxide species were detected in the $FeCeO_x$-supported catalysts. This could be due to uniform distribution of Ni and Sn metal oxides within the matrix of support by forming a homogeneous phase of the composite catalyst [16].

As is well known, the reduction treatment is necessary before the WGS reaction. Thus, all the catalysts reduced at 400 °C for 2 h using process gas, which was characterized by XRD. The XRD patterns of these reduced catalysts are illustrated in Figure 3b. The reflections obtained for all reduced catalysts evidenced the presence of (220), (311), (222), (400), (422), (511), and (440) crystal planes, corresponding to the magnetite phase (Fe_3O_4) of iron oxide (JCPDS 01-088-0315) [24]. It is obvious that the hematite phase of support transformed to magnetite phase during the reduction process. Additionally, the diffraction peaks related to CeO_2 (JCPDS 34-0394) were observed along with the magnetite phase in the XRD patterns of all reduced catalysts [22,23]. Similar to the fresh catalysts, the peaks correspond to Ni and Sn metal species were not observed in the case of $FeCeO_x$ supported Ni, Sn, and NiSn catalysts. This suggests that the Ni and Sn metal species were highly distributed in the matrix of $FeCeO_x$ support under the reduction conditions.

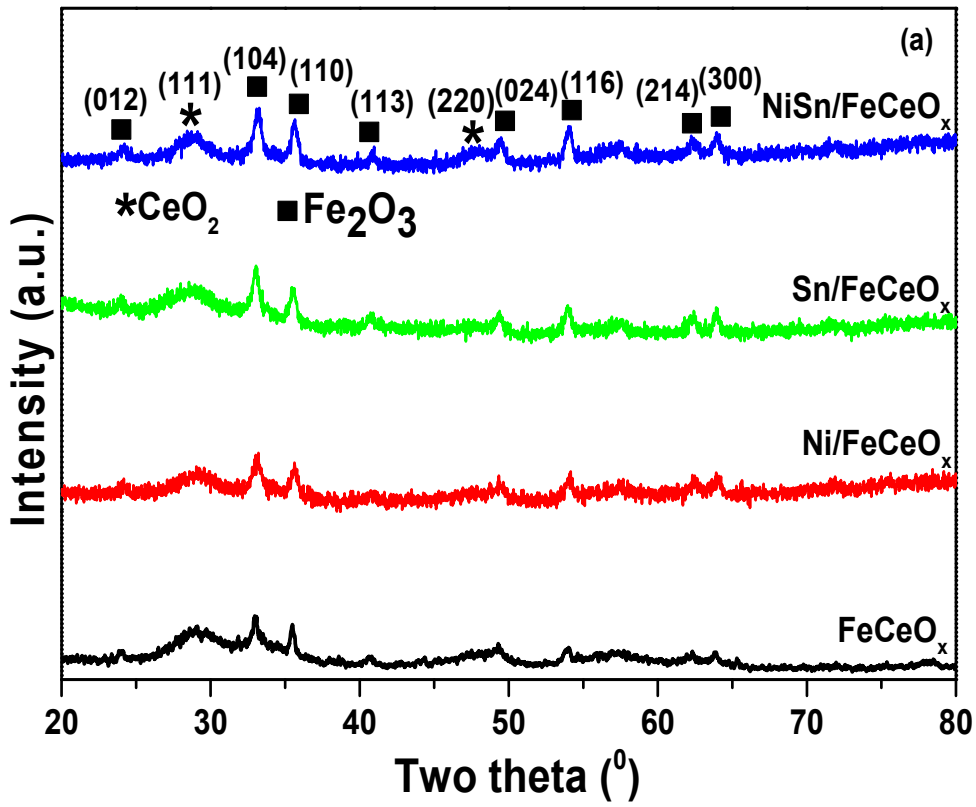

Figure 3. *Cont.*

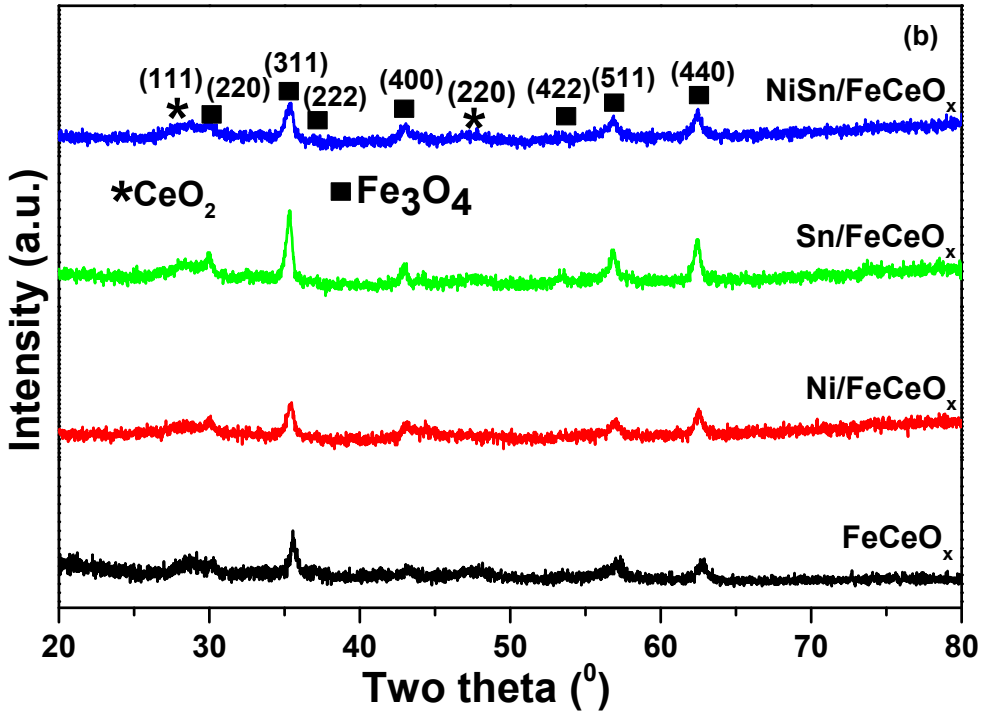

Figure 3. XRD patterns of (**a**) fresh (**b**) reduced $FeCeO_x$, $Ni/FeCeO_x$, $Sn/FeCeO_x$, and $NiSn/FeCeO_x$ catalysts.

The average crystallite size, lattice strain, and lattice parameter values were calculated using the (311), (400), (511), and (440) peaks corresponding to the magnetite phase of the reduced catalysts, and the obtained results are presented in Table 1. It is clear that the crystallite size of the magnetite phase has decreased with the deposition of Ni and NiSn over the $FeCeO_x$ support. In contrast, the crystallite size of magnetite phase has increased upon the deposition of Sn over the support. Compared to the $FeCeO_x$ sample, $FeCeO_x$-supported Ni and NiSn catalysts have higher lattice strain, while the $Sn/FeCeO_x$ possessed lower lattice strain. These findings are in good agreement with the crystallite size values, where a lower crystallite size produces higher lattice strain. From Table 1, it is also evident that the lattice parameter of the magnetite phase increased upon the deposition of monometallic Ni, Sn, and bimetallic NiSn over the $FeCeO_x$ support. This lattice expansion could be attributed to the insertion of Ni and Sn metal species into the magnetite crystal under reduction conditions.

Table 1. Size, lattice strain, and lattice parameter of $FeCeO_x$, $Ni/FeCeO_x$, $Sn/FeCeO_x$, and $NiSn/FeCeO_x$ catalysts.

Catalysts	Crystallite Size (nm) [a]	Lattice Strain [b]	Lattice Parameter (Å) [c]
$FeCeO_x$	13.0	0.011	8.3738
$Ni/FeCeO_x$	11.7	0.013	8.3931
$Sn/FeCeO_x$	15.5	0.004	8.4118
$NiSn/FeCeO_x$	10.5	0.017	8.4091

[a,b,c] Calculated from XRD of reduced catalysts.

2.2.2. BET Surface Area and Scanning Electron Microscopy/Elemental Mapping (SEM/EDS)

The Brunauer-Emmett-Teller (BET) surface areas of catalysts are summarized in Table 2. As can be observed, the surface area of $FeCeO_x$ decreased after the deposition of monometallic Ni and Sn, and bimetallic NiSn. Particularly, the surface area decreased significantly when Sn deposited over the $FeCeO_x$, which is in line with the XRD results. Moreover, the surface area of the catalysts slightly decreased from the fresh state to the reduced state. This might be due to the little agglomeration of catalyst particles during the reduction process. The surface area of bimetallic $NiSn/FeCeO_x$ is quite

higher as compared to the monometallic Ni/$FeCeO_x$ and Sn/$FeCeO_x$ catalysts. This is possibly due to the strong interface interaction between the NiSn and $FeCeO_x$ in the catalyst.

The surface morphology of fresh NiSn/$FeCeO_x$ catalyst was investigated by SEM analysis, and the corresponding image is shown in Figure 4. As can be observed, the SEM image of the catalyst exhibited an irregular morphology without observing a characteristic shape for the particles. EDS mapping was also performed to investigate the elemental constituents and distribution patterns of Ni and Sn on the surface of $FeCeO_x$. Since the catalyst contains a high amount of $FeCeO_x$ composition, Fe and Ce elements were densely found in the catalyst. Moreover, Fe was more densely distributed than Ce in the catalyst. This indicates the large quantity of Fe present in the $FeCeO_x$ support. The deposited Ni and Sn were ubiquitously detected on the $FeCeO_x$ surface, and their distribution pattern was fairly uniform. This finding confirms the homogeneous distribution of Ni and Sn within the matrix of $FeCeO_x$, which is in accordance with XRD results. The chemical composition of each metal in the fresh catalysts was determined by EDS analysis, and the results are reported in Table 2. The measured elemental composition of the catalysts using EDS is nearly the same as the nominal values.

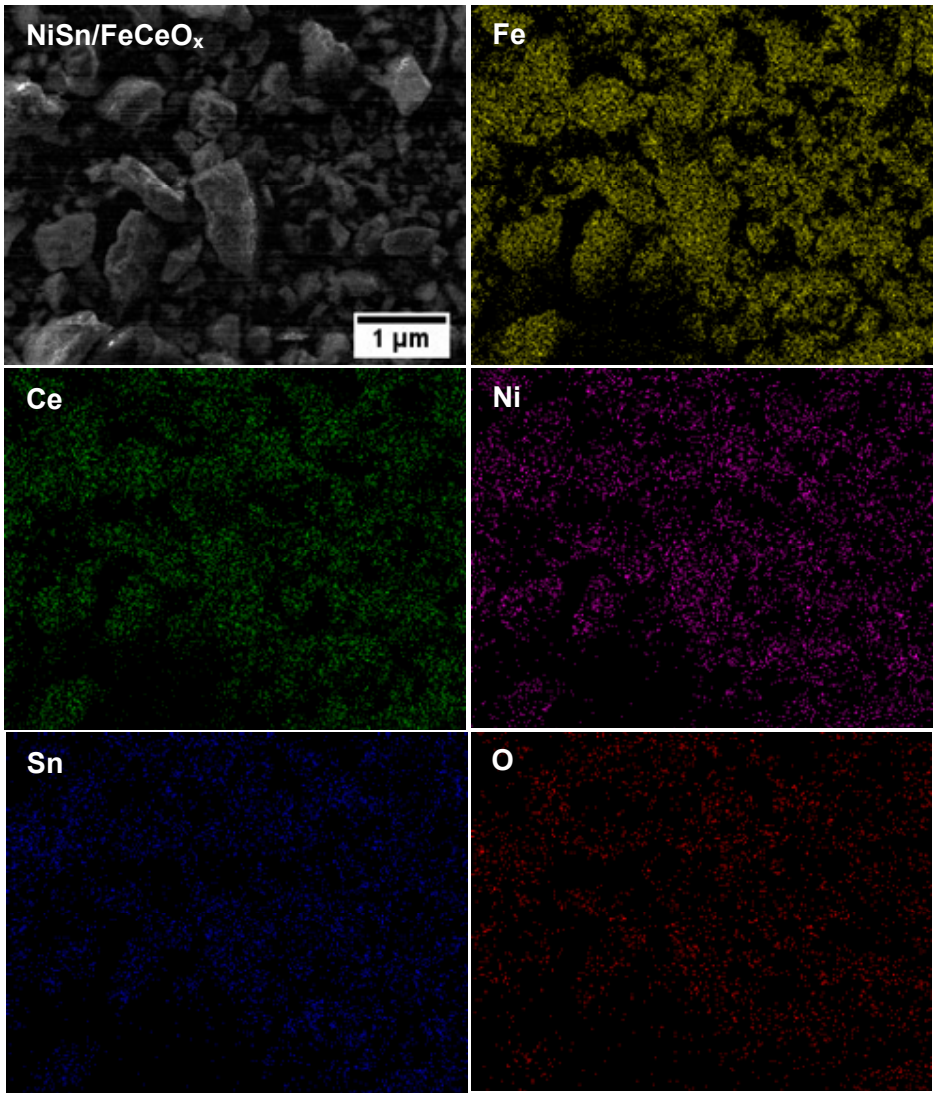

Figure 4. SEM image and elemental mapping of fresh NiSn/$FeCeO_x$ catalyst.

Table 2. Composition and Brunauer-Emmett-Teller (BET) surface area of $FeCeO_x$, $Ni/FeCeO_x$, $Sn/FeCeO_x$, and $NiSn/FeCeO_x$ catalysts.

Catalysts	Wt % [a]				BET SA (m^2/g)	
	Fe	Ce	Ni	Sn	Fresh	Reduced
$FeCeO_x$	83.82 (83.33)	16.18 (16.67)	-	-	115	101
$Ni/FeCeO_x$	74.13 (75)	15.64 (15)	10.23 (10)	-	85	73
$Sn/FeCeO_x$	74.57 (75)	14.87 (15)	-	10.56 (10)	70	62
$NiSn/FeCeO_x$	75.18 (75)	14.92 (15)	5.07 (5)	4.83 (5)	94	85

[a] Nominal values in parenthesis.

2.2.3. H_2-Temperature-Programmed Reduction (H_2-TPR) Measurement

Since it is widely recognized that the redox activity could play an important role in the HT-WGS reaction, the reducibility of fresh catalysts was investigated using the H_2-TPR technique. Figure 5 presented the H_2-TPR profiles of the catalysts. As can be seen, the reduction profile of $FeCeO_x$ catalyst can be deconvoluted into four distinct peaks at 388 °C, 554 °C, 705 °C, and 789 °C, which are assigned to the reduction of Fe_2O_3 to Fe_3O_4, surface CeO_2, Fe_3O_4 to FeO, and FeO to metallic Fe, respectively [20,25]. Similar to the $FeCeO_x$, the $Ni/FeCeO_x$, $Sn/FeCeO_x$, and $NiSn/FeCeO_x$ catalysts also exhibited three peaks for Fe_2O_3 and one peak for surface CeO_2 reduction. Since Fe_3O_4 is the active phase for the HT-WGS reaction, the reduction of hematite to magnetite could be a key step in the reduction profiles. As compared to the $FeCeO_x$, the reduction of hematite has shifted toward a lower temperature after the loading of Ni on the $FeCeO_x$, whereas the deposition of Sn over the $FeCeO_x$ has shifted the reduction peak of Fe_2O_3 toward a higher temperature. In the case of bimetallic $NiSn/FeCeO_x$ catalyst, the reduction peak of Fe_2O_3 to Fe_3O_4 shifted to a lower temperature, compared to that of the $FeCeO_x$ sample. These results clearly imply the strong synergistic interaction between the loaded metals (Ni/Sn) and $FeCeO_x$ support, where Ni promotes the reducibility of Fe_2O_3 at lower temperature while Sn favors the reduction of Fe_2O_3 at higher temperature. These findings correlate well with the XRD and BET results, where the monometallic $Sn/FeCeO_x$ catalyst showed higher crystallite size/lower stress and lower BET surface area than the monometallic $Ni/FeCeO_x$ and bimetallic $NiSn/FeCeO_x$ samples.

As compared to $FeCeO_x$, monometallic $Ni/FeCeO_x$ and $Sn/FeCeO_x$ catalysts have an additional major peak at 462 °C and 697 °C, which can be ascribed to the reduction of NiO and SnO_2, respectively. Interestingly, the combination of Ni and Sn supported on $FeCeO_x$ has significantly decreased the reduction temperature of both NiO (426 °C) and SnO_2 (647 °C) when compared to the monometallic $Ni/FeCeO_x$ and $Sn/FeCeO_x$, respectively. This improvement unambiguously confirms the strong synergistic effect between Ni and Sn in the $NiSn/FeCeO_x$ that helps to ease the reducibility of both NiO and SnO_2. This fact is in accordance with XRD data, which demonstrated the reduced crystallite size with the presence of both Ni and Sn in the catalyst. In the case of supported NiCu [3] and NiSn [16] based bimetallic samples, studies have reported the formation of CuNi and NiSn alloy from the decreased reduction temperatures, respectively. Thus, the low reduction temperatures of NiO and SnO_2 imply the formation of NiSn alloy in the $NiSn/FeCeO_x$ catalyst.

2.2.4. X-ray Photoelectron Spectroscopy (XPS) Measurement

XPS analysis was conducted to understand the electronic structure and oxidation states of the various species present over the surface of reduced catalysts. The Fe 2p XPS spectra of reduced catalysts are displayed in Figure 6a. Two distinct peaks are observed at around 710.0–711.2 eV and 723.1–724.5 eV with spin-orbit splitting energy of 13.1–13.3 eV for all samples, which corresponded to Fe $2p_{3/2}$ and Fe $2p_{1/2}$ states, respectively. Each Fe $2p_{3/2}$ and Fe $2p_{1/2}$ sublevel could be deconvoluted into two main peaks and one satellite peak. For the Fe $2p_{3/2}$ sub-band, the main peaks at 709.7–711.1 eV and 713.1–715.7 eV are ascribed to the Fe^{2+} and Fe^{3+} states, respectively, while the satellite band at 717.2–719.6 eV is attributed to both the Fe^{2+} and Fe^{3+} ions [20,26,27]. All these findings unambiguously

imply the formation of magnetite (Fe_3O_4) phase under the reduction conditions, which is consistent with XRD results. These results are also in accordance with earlier reports [20,28,29].

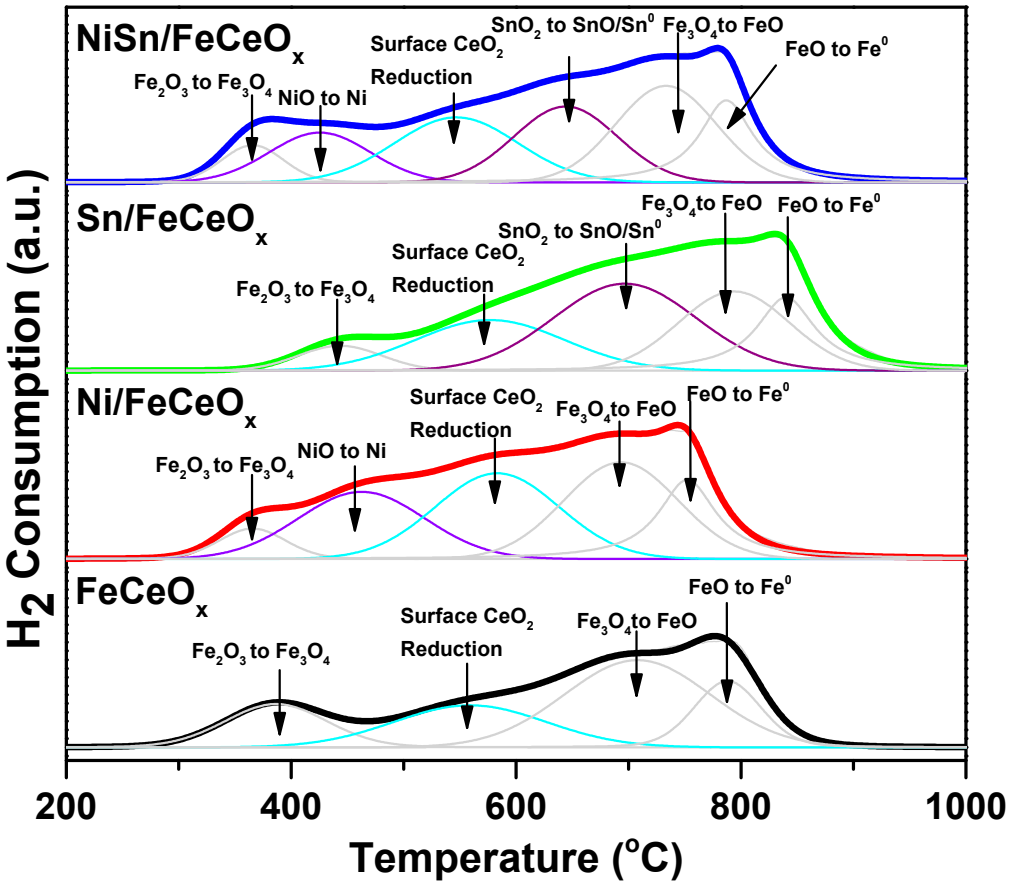

Figure 5. H_2-Temperature-Programmed Reduction (H_2-TPR) profiles of fresh $FeCeO_x$, $Ni/FeCeO_x$, $Sn/FeCeO_x$, and $NiSn/FeCeO_x$ catalysts.

The estimation of a surface Fe^{3+}/Fe^{2+} redox ratio is helpful to investigate the effect of metals deposition over the $FeCeO_x$ support extensively. Since Fe 2p XPS includes satellite peaks that could partially overlap with main peaks, the quantification of surface Fe^{2+} and Fe^{3+} species from Fe 2p spectra is not accurate. Hence, the relative Fe^{3+}/Fe^{2+} ratio over the surface of the samples was calculated precisely using Fe 3p XPS spectra as it does not have any satellites. The Fe 3p spectra of all reduced catalysts shown in Figure 6b were deconvoluted into two peaks at 54.3–55.1 eV and 55.6–56.8 eV, which were assigned to the Fe^{2+} and Fe^{3+} ions, respectively. The relative ratio of Fe^{3+}/Fe^{2+} was estimated from the corresponding integrated peak areas, and the obtained results were listed in Table 3. The relative Fe^{3+}/Fe^{e2+} concntration was found to be 1.65, 1.78, 1.76, and 1.80 for $FeCeO_x$, $Ni/FeCeO_x$, $Sn/FeCeO_x$, and $NiSn/FeCeO_x$ catalysts, respectively. Typically, the stoichiometric Fe_3O_4 phase shows the Fe^{3+}/Fe^{2+} ratio of 2. Thus, the lower Fe^{3+}/Fe^{2+} ratio below 2 in all the reduced catalysts could be due the formation of nonstoichiometric Fe_3O_4 with the modification of magnetite lattice by dopants, which is in agreement with previous reports [20,29]. As can be noted from Table 3, the surface Fe^{3+}/Fe^{2+} ratio increased when Ni and/or Sn deposited on the $FeCeO_x$ support. Furthermore, the binding energy of Fe 2p and Fe 3p peaks has shifted to a higher region with the loading of metals (Ni and/or Sn) on the $FeCeO_x$ support. These findings obviously suggest that the Fe component of the support has strongly interacted with deposited metals, which is in harmony with XRD and H_2-TPR results.

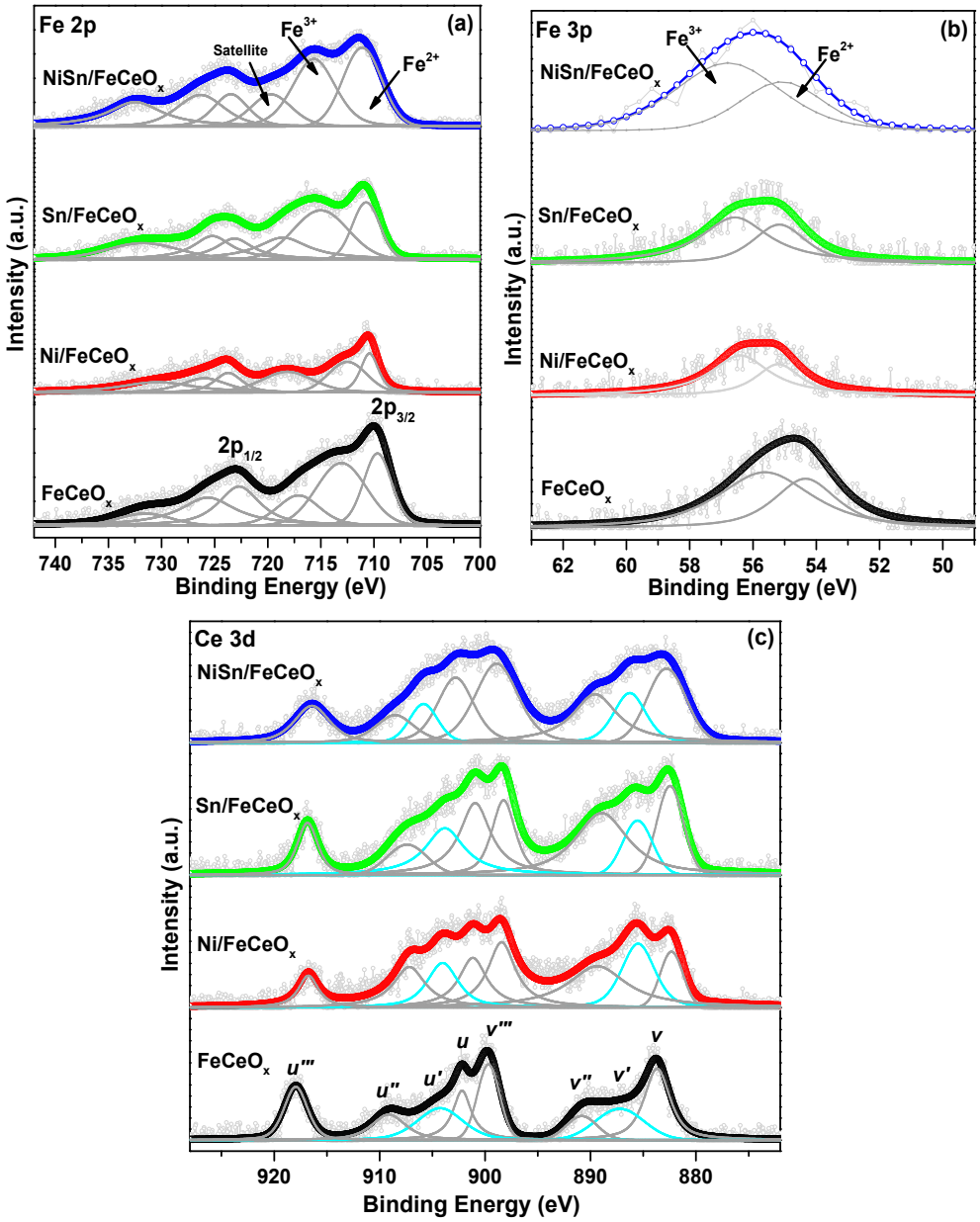

Figure 6. (**a**) Fe 2p (**b**) Fe 3p, and (**c**) Ce 3d XPS spectra of reduced $FeCeO_x$, $Ni/FeCeO_x$, $Sn/FeCeO_x$, and $NiSn/FeCeO_x$ catalysts.

Table 3. Surface Fe^{3+}/Fe^{2+}, Ce^{4+}/Ce^{3+}, Ni^0/Ni^{2+}, and $Sn^0/Sn^{2+}+Sn^{4+}$ ratio of reduced $FeCeO_x$, $Ni/FeCeO_x$, $Sn/FeCeO_x$, and $NiSn/FeCeO_x$ catalysts.

Catalysts	Fe^{3+}/Fe^{2+}	Ce^{4+}/Ce^{3+}	Ni^0/Ni^{2+}	$Sn^0/Sn^{2+}+Sn^{4+}$
$FeCeO_x$	1.65	2.77	-	-
$Ni/FeCeO_x$	1.78	2.94	0.32	-
$Sn/FeCeO_x$	1.76	3.57	-	0.12
$NiSn/FeCeO_x$	1.80	5.26	0.45	0.32

Figure 6c displays the Ce 3d core-level spectra of reduced catalysts. As shown in Figure 6c, the Ce 3d peaks of the samples can be fit into four sets of spin-orbit doublets, in which the peaks labeled as v, v′, v′′, and v′′′ represented the $3d_{5/2}$ sublevel, while the signals labeled u, u′, u′′, and u′′′ referred to the $3d_{3/2}$ state. Moreover, the u, u′′, u′′′, v, v′′, and v′′′ peaks are ascribed to Ce^{4+} ions, whereas u′ and v′ are

corresponding to Ce^{3+} ions [24,29,30]. Hence, both the Ce^{3+} and Ce^{4+} states are present on the surfaces of all the reduced catalysts. The relative surface quantity of Ce^{4+}/Ce^{3+} on the surface of the reduced catalysts is illustrated in Table 3. The surface Ce^{4+}/Ce^{3+} ratio has enhanced with the deposition of Ni and/or Sn metals over the $FeCeO_x$ support. Moreover, with the loading of Ni and/or Sn components on the $FeCeO_x$, the binding energy of the Ce 3d peak shifted to a lower region. These observations clearly indicate the strong interaction between the Ce components of the support and loaded metal/s, which is corroborated with Fe XPS results.

The Ni $2p_{3/2}$ spectra of the reduced monometallic $Ni/FeCeO_x$ and bimetallic $NiSn/FeCeO_x$ catalysts are shown in Figure 7a. The Ni $2p_{3/2}$ spectra of the samples can be divided into two main peaks and a satellite peak. The main peak at lower binding energy (approximately 852.5 eV) is indexed to the metallic Ni^0 state, while the other main peak at higher binding energy (approximately 855.4 eV) is associated to a Ni^{2+} ion [10]. The XPS spectra of Sn 3d for the reduced monometallic $Sn/FeCeO_x$ and bimetallic $NiSn/FeCeO_x$ catalysts are depicted in Figure 7b. The Sn 3d spectra of the samples is composed of two well-defined peaks at 486.1–486.5 eV and 494.5–494.9 eV, which are ascribed to the Sn $3d_{5/2}$ and Sn $3d_{3/2}$ states, respectively. By peak fitting, the Sn $3d_{5/2}$ sublevel could be separated into three peaks. The first peak at around 485.0 eV can be assigned to metallic Sn^0, the second peak at around 486.5 eV belong to an Sn^{2+} ion, while the third peak at around 487.6 eV is associated with an Sn^{4+} ion [16]. The formation of metallic Ni^0 and Sn^0 states could have mainly resulted from the reduction treatment. The coexistence of ionic and metallic states of Ni and Sn together with the Fe^{3+}/Fe^{2+} and Ce^{4+}/Ce^{3+} redox couple is indicative of the synergistic interaction between the support and deposited elements through the redox equilibrium of $Fe^{2+}/Ce^{3+} + Sn^{n+}/Ni^{2+} \leftrightarrow Fe^{3+}/Ce^{4+} + Sn^0/Ni^0$.

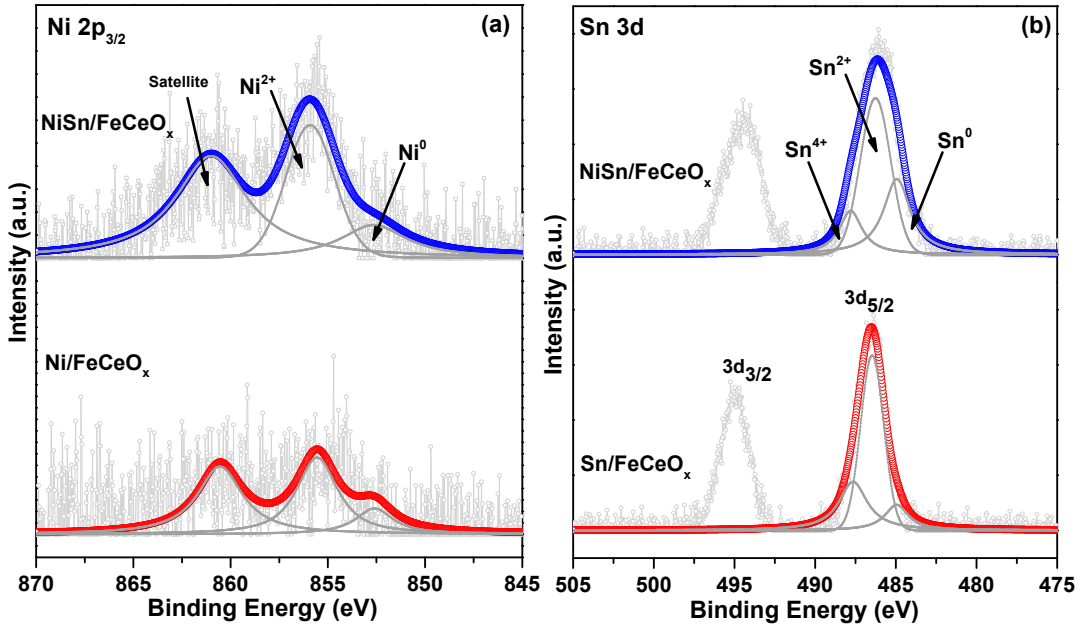

Figure 7. (**a**) Ni 2p and (**b**) Sn 3d XPS spectra of reduced $Ni/FeCeO_x$ and $Sn/FeCeO_x$ catalysts, respectively.

The concentration of Ni^0/Ni^{2+} and Sn^0/Sn^{n+} ratios were quantified, and the corresponding values are presented in Table 3. It is noteworthy that the Ni^0/Ni^{2+} and Sn^0/Sn^{n+} ratios increased obviously from monometallic $Ni/FeCeO_x$ and $Sn/FeCeO_x$ catalysts to bimetallic $NiSn/FeCeO_x$ catalyst, respectively. This may imply the possibility of NiSn alloy formation on the surface bimetallic $NiSn/FeCeO_x$ catalyst. The Ni 2p of bimetallic NiSn/ $FeCeO_x$ showed a shift toward higher binding energy as compared to monometallic $Ni/FeCeO_x$ catalysts. In contrast, the Sn 3d of bimetallic $NiSn/FeCeO_x$ has shifted to lower binding energy in comparison to monometallic $Sn/FeCeO_x$ catalysts. These findings provide firm evidence for a strong interaction between Ni and Sn species, which infers an electron density increase on

the Sn nucleus and decrease on the Ni nucleus. A similar peak shift trend was also reported in the case of bimetallic CuNi/Fe_2O_3 catalysts [3], in which the CuNi/Fe_2O_3 showed an upward shift in Ni 2p binding energy and a downward shift in Cu 2p binding energy when compared to monometallic Ni/Fe_2O_3 and Cu/Fe_2O_3 catalysts, respectively. From the above observation, studies have confirmed the formation of CuNi alloy in the bimetallic CuNi/Fe_2O_3 catalyst. Thus, in the present investigation, the shifts in the binding energy of Ni 2p and Sn 3d peaks unambiguously suggest the formation of NiSn alloy over the surface of bimetallic NiSn/$FeCeO_x$ catalysts. This fact was also confirmed from the H_2-TPR findings.

The O 1s core level XPS spectra of reduced catalysts are displayed in Figure 8. As shown in Figure 8, the O 1s spectra can be divided into three peaks, which are corresponding to the different oxygen species present on the surface of the catalysts. The first peak (O_α) at approximately 529.0 eV corresponds to lattice oxygen (O^{2-}), the second peak (O_β) at approximately 530.3 eV can be assigned to adsorbed oxygen species or defective oxygen species (O_2^{2-} or O^-), while the third peak ($O\gamma$) at approximately 532.6 eV can be attributed to chemisorbed oxygen species from surface hydroxyl or carbonate species [31,32].

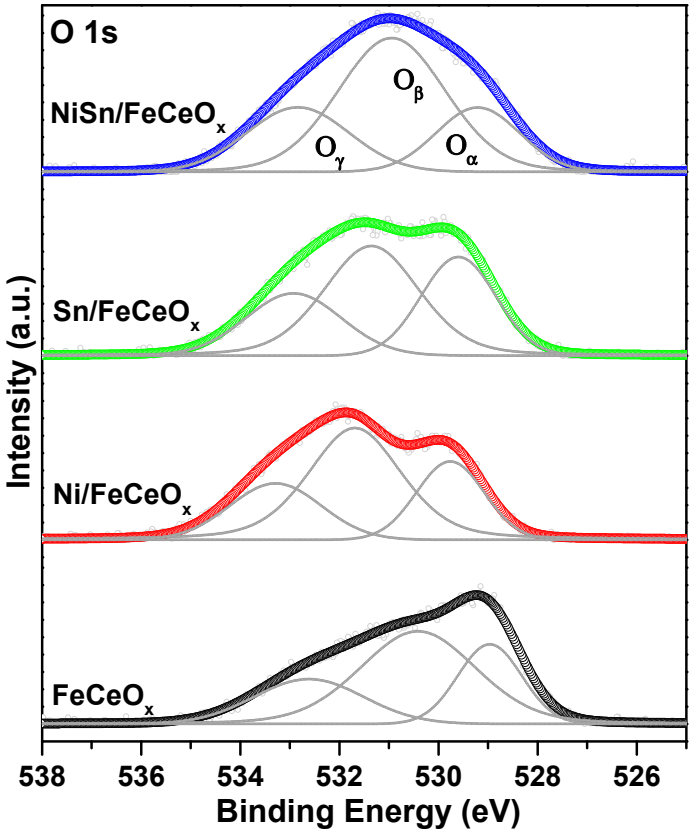

Figure 8. O 1s XPS spectra of reduced $FeCeO_x$, Ni/$FeCeO_x$, Sn/$FeCeO_x$, and NiSn/$FeCeO_x$ catalysts.

With the loading of Ni and/or Sn on the $FeCeO_x$, the binding energy of O_α, O_β, and $O\gamma$ peaks have shifted toward higher regions as compared to the $FeCeO_x$ catalyst. This trend in the peaks' shift can be explained in terms of the electronegativity of elements in the catalysts. The electronegativity of Ni (1.91) and Sn (1.96) is greater than the Fe (1.83) and Ce (1.12), so the electron affinity of Ni and Sn is stronger than the $FeCeO_x$ support, which leads to the higher binding energy of O 1s in monometallic Ni/$FeCeO_x$, Sn/$FeCeO_x$, and bimetallic NiSn/$FeCeO_x$ compared with the $FeCeO_x$ due to the lower electron density around the O element [33,34]. This finding indicates the synergistic interaction between $FeCeO_x$ and deposited metals (Ni/Sn), which correlates well with the Ni 2p and Sn 3d XPS results.

2.3. Structure–Activity Relationship

The loading of Ni on $FeCeO_x$ has improved the WGS performance at temperature below 550 °C, while the deposition of Sn on $FeCeO_x$ has enhanced the activity at above 550 °C. Upon the addition of Ni together with Sn to $FeCeO_x$, the CO conversion in WGS is greatly enhanced as compared to the $FeCeO_x$ in the whole tested temperature range. Moreover, the $NiSn/FeCeO_x$ catalyst showed good time-on-stream stability without any methanation reaction, even at steam-to-CO ratios as low as 0.8.

Typically, the adsorption and activation of reactants (CO and H_2O) could play a key role on the WGS [20,35]. As reported in the literature [20,36], the lattice strain could impact the activation energy barriers for bond-making and bond-breaking events on the surface of catalysts, where the high lattice strain can augment the WGS activity. It can be noticed that the bimetallic $NiSn/FeCeO_x$ catalyst with highest lattice strain showed the best activity among the $Ni/FeCeO_x$, $Sn/FeCeO_x$, and $FeCeO_x$ samples (Table 1). As compared to the $FeCeO_x$, the lattice strain is enhanced when Ni deposited on $FeCeO_x$, while it is decreased after the loading of Sn over the $FeCeO_x$ (Table 1). At temperatures below 550 °C, the WGS activity trend of $FeCeO_x$, $Ni/FeCeO_x$, and $Sn/FeCeO_x$ catalysts correlated well with the trend in lattice strain. However, at above 550 °C, the $Sn/FeCeO_x$ catalyst with lower lattice strain exhibited higher performance than the $Ni/FeCeO_x$ and $FeCeO_x$ samples. Thus, it can be concluded that the lattice strain might not be a decisive factor for the WGS activity of catalysts in the present investigation.

On the other hand, the Fe_3O_4 phase of iron-based catalysts has been identified as an active phase for WGS reaction [3,20,37]. Hence, the reducibility of support from hematite to magnetite phase could play a crucial role in HT-WGS. As compared to the $FeCeO_x$, the deposition of Ni on $FeCeO_x$ shifted the $Fe_2O_3 \rightarrow Fe_3O_4$ reduction to a lower temperature, whereas the loading of Sn on $FeCeO_x$ moved the hematite reduction to a higher temperature (H_2-TPR). This trend is a consequence of metal–support interactions that decide the catalytic performance of the supported metals. Comparing activity results with the reducibility of the catalysts, it appeared that the WGS performance of the catalysts at temperatures below 550 °C correlated with the reduction temperature of the hematite phase of their support. However, as compared to the $FeCeO_x$ at a higher temperature above 550 °C, the monometallic $Ni/FeCeO_x$ exhibited lower performance, while monometallic $Sn/FeCeO_x$ had greater activity. Although the bimetallic $NiSn/FeCeO_x$ and monometallic $Ni/FeCeO_x$ catalysts have similar temperatures for the reduction of hematite phase, the $NiSn/FeCeO_x$ showed the best WGS activity among all catalysts within the temperature range studied. These findings pointing out that regardless of the reducibility of support, the deposited metals could play a critical role in generating the active centers for WGS on the surface of the catalysts [38]. At temperatures below 550 °C, the higher activity of $Ni/FeCeO_x$ than the $FeCeO_x$ could be due to the metallic Ni phase that formed on $FeCeO_x$ from the reduction of NiO. Moreover, the higher activity of $Ni/FeCeO_x$ catalyst is accompanied by the methane formation. Typically, the large metallic Ni particles present on the surface of a catalyst can promote the production of methane [3,39]. Hence, the methanation activity of $Ni/FeCeO_x$ in WGS could be due to the formation of bulk metallic Ni particles over the surface of the catalyst. However, the lower activity of $Ni/FeCeO_x$ catalyst in comparison to the $FeCeO_x$ sample at a temperature above 550 °C may be caused by the sintering of the active metallic Ni phase and/or the carbon deposition on the metallic nickel blocking the active sites on the surface. On the other hand, the greater performance of the $Sn/FeCeO_x$ catalyst than the $FeCeO_x$ sample at a temperature above 550 °C might have resulted from the activation of the Sn metallic phase at higher temperatures. Although the bimetallic $NiSn/FeCeO_x$ catalyst has Ni, it exhibited superior activity in the whole investigated temperature range as well as excellent stability without the methanation reaction even under a low steam-to-CO ratio of 0.8. The strong synergistic effect between Ni and Sn, evidenced from the H_2-TPR and XPS, could help reduce the particle size of agglomerated metallic Ni particles by forming the NiSn alloy over the surface of $NiSn/FeCeO_x$ catalysts [16]. This fact was confirmed clearly with the absence of methanation reaction over the $NiSn/FeCeO_x$ catalyst during the WGS. Thus, the deposition of Ni together with Sn on $FeCeO_x$ not only increased the catalyst activity but also suppressed the methanation due to the formation of NiSn alloy on the catalyst surface [14,15].

It is widely accepted that besides the leading role of a metallic phase, the WGS requires the participation of a metal–metal oxide support interface [40–42]. The synergistic effect between the deposited metals and the support through the redox equilibrium of $Fe^{2+}/Ce^{3+} + Sn^{n+}/Ni^{2+} \leftrightarrow Fe^{3+}/Ce^{4+} + Sn^{0}/Ni^{0}$ was found to exist in the Ni/$FeCeO_x$, Sn/$FeCeO_x$, and NiSn/$FeCeO_x$ catalysts (XPS). As compared to the monometallic Ni/$FeCeO_x$ and Sn/$FeCeO_x$, the higher surface Fe^{3+}/Fe^{2+}, Ce^{4+}/Ce^{3+}, Ni^{0}/Ni^{2+}, and Sn^{0}/Sn^{n+} ratios over the bimetallic NiSn/$FeCeO_x$ catalyst (Table 3) indicates the strong interface interaction between NiSn and $FeCeO_x$ in the catalyst. This could be also responsible for the best WGS activity of bimetallic NiSn/$FeCeO_x$. Thus, the superior performance of the bimetallic NiSn/$FeCeO_x$ catalyst could stem from the combined contributions of its highest lattice strain, NiSn alloy phase, and strong synergistic redox interaction between the deposited NiSn and the $FeCeO_x$ support interface, as supported by XRD, H_2-TPR, and XPS results, respectively.

3. Materials and Methods

3.1. Synthesis of Catalysts

The $FeCeO_x$ support with an atomic ratio of 10:2 was synthesized by the co-precipitation method. First, the desired amount of $Fe(NO_3)_3{\cdot}9H_2O$ (Sigma-Aldrich, St. Louis, MO, USA) and $(NH_4)_2Ce(NO_3)_6$ (Sigma-Aldrich) precursors were dissolved separately in distilled water and mixed together at room temperature. Then, aqueous NH_3 was added dropwise to this solution until the pH reached 9.0 under continuous stirring. The resulting precipitate was filtered and washed with deionized water. Then, the solid mixture was dried at 100 °C for 12 h and calcined at 500 °C for 3 h.

The incipient wetness impregnation method was used to prepare the monometallic Ni/$FeCeO_x$ and Sn/$FeCeO_x$ and bimetallic NiSn/$FeCeO_x$ catalysts. In a typical synthesis, an aqueous solution containing the required amount of $Ni(NO_3)_2.6H_2O$ (Sigma-Aldrich) and/or $SnCl_4.5H_2O$ (Sigma-Aldrich) precursors was mixed with the requisite amount of $FeCeO_x$ support obtained through the co-precipitation method. Then, the mixed solution was stirred at 80 °C until the water was fully vaporized. Finally, the obtained solid product was oven dried at 100 °C for 12 h and calcined at 500 °C for 3 h. The loading of Ni and/or Sn was 10% by weight on $FeCeO_x$. The weight percentage ratio of Ni and Sn in the bimetallic NiSn/$FeCeO_x$ catalyst was 1:1.

3.2. Catalysts Characterizations

Powder X-ray diffraction patterns were recorded over a 2θ angle range of 20–80° with a step size of 0.02° using a Rigaku Multiflex diffractometer (Cu-Kα radiation, Cincinnati, OH, USA). Brunauer-Emmett-Teller (BET) surface areas of the catalysts were determined from N_2 adsorption/desorption isotherms recorded at 77 K on a Micromeritics 2010 instrument (Cincinnati, OH, USA). SEM image and EDS mapping of the catalysts was done by using FEI XL-30 microscope (Cincinnati, OH, USA) with an operating voltage of 200 kV. H_2-temperature programmed reduction (H_2-TPR) was carried out by passing 10% H_2/He up to a temperature of 1000 °C at a rate of 5 °C min^{-1} using AutoChem II 2910 (Micromeritics, Cincinnati, OH, USA). X-ray photoelectron spectroscopy (XPS) analysis was performed on a Thermo Scientific spectrometer (Cincinnati, OH, USA) equipped using monochromatic Al-Kα (hν = 1486.7 eV) radiation source. All spectra were corrected based on the carbon (C 1 s) peak at 284.6 eV.

3.3. Catalytic Activity Measurements

The WGS performance of catalysts was tested in a fixed-bed quartz reactor from 450 to 600 °C at atmospheric pressure. Prior to the reaction, the catalyst (0.1 g) was reduced in situ at 400 °C for 2 h in a flow of process gas (process gas is a mixture of H_2, CO, CO_2 (99.9% pure gases), and water vapor) with a reductant-to-oxidant ratio of R = 1.4 {R = ([CO] + [H_2])/([CO_2] + [H_2O])}. The deionized water was supplied through an ISCO series D pump controller and vaporized at 150 °C using heating tape before entering the reactor. The resulting water vapor was mixed with reactant gas (CO) at a steam-to-CO ratio of 1.5 and a GHSV of 60,000 h^{-1}. The measurements were taken when the reaction reached steady

state, and three data points were recorded at each temperature. The reaction effluent was analyzed online using a GC (Gow-Mac series 550, Cincinnati, OH, USA) using a porapak Q column and thermal conductivity detector. The time-on-stream stability experiments were performed for 50 h at 500 °C, steam-to-CO ratios of 1.5 and 0.8, and GHSV of 60,000 h^{-1}.

4. Conclusions

The influence of monometallic (Ni or Sn) and bimetallic (NiSn) deposition on the HT-WGS activity of $FeCeO_x$ has been studied. The addition of bimetallic NiSn has greatly enhanced the catalytic performance of $FeCeO_x$ in comparison to the monometallic Ni and Sn loadings. The bimetallic $NiSn/FeCeO_x$ catalyst was also showed stable performance with time-on-stream for 50 h of the reaction and the effective suppression of the methanation even under the low steam-to-CO ratio of 0.8. The coexistence of Ni and Sn on $FeCeO_x$ led to the formation of NiSn alloy and a strong metal–support interaction between the NiSn and $FeCeO_x$ mixed oxide support interface. These observations in the $NiSn/FeCeO_x$ catalyst were found to play a decisive role in achieving its superior activity and stability in the HT-WGS reaction. Considering the promising attributes mentioned above in combination with the economic feasibility of this novel catalytic system, it can be concluded that the $NiSn/FeCeO_x$ catalyst constitutes a potential alternative for the commercial Cr-based HT-WGS catalyst.

Author Contributions: Conceptualization, D.D.; Data curation, D.D.; Formal analysis, D.D.; Investigation, D.D.; Supervision, P.G.S.; Validation, D.D. and P.G.S.; Writing—original draft, D.D.; Review and editing, D.D. and P.G.S. All authors have read and agreed to the published version of the manuscript.

Funding: This research received no external funding.

Conflicts of Interest: The authors declare no conflict of interest.

References

1. Vovchok, D.; Guild, C.J.; Dissanayake, S.; Llorca, J.; Stavitski, E.; Liu, Z.; Palomino, R.M.; Waluyo, I.; Li, Y.; Frenkel, A.I.; et al. *In Situ* Characterization of Mesoporous Co/CeO_2 Catalysts for the High-Temperature Water-Gas Shift. *J. Phys. Chem. C* **2018**, *122*, 8998–9008. [CrossRef]
2. Dincer, I.; Acar, C. Review and Evaluation of Hydrogen Production Methods for Better Sustainability. *Int. J. Hydrog. Energy* **2015**, *40*, 11094–11111. [CrossRef]
3. Jha, A.; Jeong, D.-W.; Shim, J.-O.; Jang, W.-J.; Lee, Y.-L.; Rode, C.V.; Roh, H.-S. Hydrogen Production by the Water-Gas Shift Reaction using $CuNi/Fe_2O_3$ Catalyst. *Catal. Sci. Technol.* **2015**, *5*, 2752–2760. [CrossRef]
4. Ratnasamy, C.; Wagner, J.P. Water Gas Shift Catalysis. *Catal. Rev.* **2009**, *51*, 325–440. [CrossRef]
5. Lee, D.-W.; Lee, M.S.; Lee, J.Y.; Kim, S.; Eom, H.-J.; Moon, D.J.; Lee, K.-Y. The Review of Cr-Free Fe-based Catalysts for High-Temperature Water-Gas Shift Reactions. *Catal. Today* **2013**, *210*, 2–9. [CrossRef]
6. Damma, D.; Smirniotis, P.G. Recent Advances in Iron-Based High-Temperature Water-Gas Shift Catalysis for Hydrogen Production. *Curr. Opin. Chem. Eng.* **2018**, *21*, 103–110. [CrossRef]
7. Hakeem, A.A.; Vásquez, R.S.; Rajendran, J.; Li, M.; Berger, R.J.; Delgado, J.J.; Kapteijn, F.; Makkee, M. The Role of Rhodium in the Mechanism of the Water–Gas Shift over Zirconia Supported Iron Oxide. *J. Catal.* **2014**, *313*, 34–45. [CrossRef]
8. Ashok, J.; Wai, M.H.; Kawi, S. Nickel-based Catalysts for High-temperature Water Gas Shift Reaction-Methane Suppression. *ChemCatChem* **2018**, *10*, 3927–3942. [CrossRef]
9. Lin, J.-H.; Biswas, P.; Guliants, V.V.; Misture, S. Hydrogen Production by Water–Gas Shift Reaction over Bimetallic Cu–Ni Catalysts Supported on La-Doped Mesoporous Ceria. *Appl. Catal. A Gen.* **2010**, *387*, 87–94. [CrossRef]
10. Saw, E.T.; Oemar, U.; Tan, X.R.; Du, Y.; Borgna, A.; Hidajat, K.; Kawi, S. Bimetallic Ni–Cu Catalyst Supported on CeO_2 for High-Temperature Water–Gas Shift Reaction: Methane Suppression *via* Enhanced CO Adsorption. *J. Catal.* **2014**, *314*, 32–46. [CrossRef]
11. Saw, E.T.; Oemar, U.; Ang, M.L.; Hidajat, K.; Kawi, S. Highly Active and Stable Bimetallic Nickel–Copper Core–Ceria Shell Catalyst for High-Temperature Water–Gas Shift Reaction. *ChemCatChem* **2015**, *7*, 3358–3367. [CrossRef]

12. Chayakul, K.; Srithanratana, T.; Hengrasmee, S. Catalytic Activities of Re–Ni/CeO_2 Bimetallic Catalysts for Water Gas Shift Reaction. *Catal. Today* **2011**, *175*, 420–429. [CrossRef]
13. Watanabe, K.; Miyao, T.; Higashiyama, K.; Yamashita, H.; Watanabe, M. Preparation of a Mesoporous Ceria–Zirconia Supported Ni–Fe Catalyst for the High Temperature Water–Gas Shift Reaction. *Catal. Commun.* **2011**, *12*, 976–979. [CrossRef]
14. Cerveny, L. (Ed.) Catalytic Hydrogenation. In *Studies in Surface Science and Catalysis*; Elsevier: New York, NY, USA, 1986; Volume 27, pp. 1–677.
15. Masai, M.; Honda, K.; Kubota, A.; Ohnaka, S.; Nishikawa, Y.; Nakahara, K.; Kishi, K.; Ikeda, S. Dehydrogenation and Hydrogenation Activity of Palladium-Tin-Silica and Nickel-Tin-Silica. *J. Catal.* **1977**, *50*, 419–428. [CrossRef]
16. Hengne, A.M.; Samal, A.K.; Enakonda, L.R.; Harb, M.; Gevers, L.E.; Anjum, D.H.; Hedhili, M.N.; Saih, Y.; Huang, K.-W.; Basset, J.-M. Ni−Sn-Supported ZrO_2 Catalysts Modified by Indium for Selective CO_2 Hydrogenation to Methanol. *ACS Omega* **2018**, *3*, 3688–3701. [CrossRef] [PubMed]
17. Huber, G.W.; Shabaker, J.; Dumesic, J. Raney Ni-Sn Catalyst for H_2 Production from Biomass-derived Hydrocarbons. *Science* **2003**, *300*, 2075–2077. [CrossRef] [PubMed]
18. Wang, T.; Porosoff, M.D.; Chen, J.G. Effects of Oxide Supports on the Water-Gas Shift Reaction over Pt−Ni Bimetallic Catalysts: Activity and Methanation Inhibition. *Catal. Today* **2014**, *233*, 61–69. [CrossRef]
19. Reddy, G.K.; Gunasekara, K.; Boolchand, P.; Smirniotis, P.G. Cr- and Ce-Doped Ferrite Catalysts for the High Temperature Water-Gas Shift Reaction: TPR and Mossbauer Spectroscopic Study. *J. Phys. Chem. C* **2011**, *115*, 920–930. [CrossRef]
20. Damma, D.; Jampaiah, D.; Welton, A.; Boolchand, P.; Arvanitis, A.; Dong, J.; Smirniotis, P.G. Effect of Nb Modification on the Structural and Catalytic Property of Fe/Nb/M (M = Mn, Co, Ni, and Cu) Catalyst for High Temperature Water-Gas Shift Reaction. *Catal. Today* **2019**. [CrossRef]
21. Jha, A.; Jeong, D.-W.; Jang, W.-J.; Rode, C.V.; Roh, H.-S. Mesoporous NiCu–CeO_2 Oxide Catalysts for High-Temperature Water–Gas Shift Reaction. *RSC Adv.* **2015**, *5*, 1430–1437. [CrossRef]
22. Devaiah, D.; Thrimurthulu, G.; Smirniotis, P.G.; Reddy, B.M. Nanocrystalline Alumina-Supported Ceria–Praseodymia Solid Solutions: Structural Characteristics and Catalytic CO Oxidation. *RSC Adv.* **2016**, *6*, 44826–44837. [CrossRef]
23. Devaiah, D.; Reddy, L.H.; Kuntaiah, K.; Reddy, B.M. Design of Novel Ceria-Based Nano-Oxides for CO Oxidation and Other Catalytic Applications. *Indian J. Chem.* **2012**, *51A*, 186–195.
24. Devaiah, D.; Smirniotis, P.G. Effects of the Ce and Cr Contents in Fe−Ce−Cr Ferrite Spinels on the High-Temperature Water−Gas Shift Reaction. *Ind. Eng. Chem. Res.* **2017**, *56*, 1772–1781. [CrossRef]
25. Wang, H.; Qu, Z.; Xie, H.; Maeda, N.; Miao, L.; Wang, Z. Insight Into the Mesoporous $Fe_xCe_{1-x}O_{2-\delta}$ Catalysts for Selective Catalytic Reduction of NO with NH_3: Regulable Structure and Activity. *J. Catal.* **2016**, *338*, 56–67. [CrossRef]
26. Li, G.; Li, R.; Zhou, W. A Wire-Shaped Supercapacitor in Micrometer Size Based on Fe_3O_4 Nanosheet Arrays on Fe Wire. *Nano Micro Lett.* **2017**, *9*, 46. [CrossRef] [PubMed]
27. Barbieri, A.; Weiss, W.; Van Hove, M.A.; Somorjai, G.A. Magnetite Fe_3O_4(111): Surface Structure by LEED Crystallography and Energetic. *Surf. Sci.* **1994**, *302*, 259–279. [CrossRef]
28. Jeong, D.-W.; Jha, A.; Jang, W.-J.; Han, W.-B.; Roh, H.-S. Performance of Spinel Ferrite Catalysts Integrated with Mesoporous Al_2O_3 in the High Temperature Water–Gas Shift Reaction. *Chem. Eng. J.* **2015**, *265*, 100–109. [CrossRef]
29. Damma, D.; Boningari, T.; Smirniotis, P.G. High-Temperature Water-Gas Shift over Fe/Ce/Co Spinel Catalysts: Study of the Promotional Effect of Ce and Co. *Mol. Catal.* **2018**, *451*, 20–32. [CrossRef]
30. Andana, T.; Piumetti, M.; Bensaid, S.; Russo, N.; Fino, D.; Pirone, R. Nanostructured Ceria-Praseodymia Catalysts for Diesel Soot Combustion. *Appl. Catal. B Environ.* **2016**, *197*, 125–137. [CrossRef]
31. Shim, J.-O.; Na, H.-S.; Jha, A.; Jang, W.J.; Jeong, D.-W.; Nah, I.W.; Jeon, B.-H.; Roh, H.-S. Effect of Preparation Method on the Oxygen Vacancy Concentration of CeO_2-Promoted Cu/γ-Al_2O_3 Catalysts for HTS Reactions. *Chem. Eng. J.* **2016**, *306*, 908–915. [CrossRef]
32. Kouotou, P.M.; Vieker, H.; Tian, Z.Y.; Ngamou, P.H.T.; Kasmi, A.E.; Beyer, A.; Gölzhäuser, A.; Kohse-Höinghaus, K. Structure–Activity Relation of Spinel-Type Co–Fe Oxides for Low-Temperature CO Oxidation. *Catal. Sci. Technol.* **2014**, *4*, 3359–3367. [CrossRef]

33. Yao, X.; Xiong, Y.; Zou, W.; Zhang, L.; Wu, S.; Dong, X.; Gao, F.; Deng, Y.; Tang, C.; Chen, Z.; et al. Correlation Between the Physicochemical Properties and Catalytic Performances of $Ce_xSn_{1-x}O_2$ Mixed Oxides for NO Reduction by CO. *Appl. Catal. B Environ.* **2014**, *144*, 152–165. [CrossRef]
34. Xu, X.; Zhang, R.; Zeng, X.; Han, X.; Li, Y.; Liu, Y.; Wang, X. Effects of La, Ce, and Y Oxides on SnO_2 Catalysts for CO and CH_4 Oxidation. *ChemCatChem* **2013**, *5*, 2025–2036. [CrossRef]
35. Azzam, K.G.; Babich, I.V.; Seshan, K.; Lefferts, L. Bifunctional Catalysts for Single-Stage Water–Gas Shift Reaction in Fuel Cell Applications.: Part 1. Effect of the Support on the Reaction Sequence. *J. Catal.* **2007**, *251*, 153–162. [CrossRef]
36. Grabow, L.; Xu, Y.; Mavrikakis, M. Lattice Strain Effects on CO Oxidation on Pt(111). *Phys. Chem. Chem. Phys.* **2006**, *8*, 3369–3374. [CrossRef] [PubMed]
37. Ye, Y.; Wang, L.; Zhang, S.; Zhu, Y.; Shan, J.; Tao, F. The Role of Copper in Catalytic Performance of a Fe–Cu–Al–O Catalyst for Water Gas Shift Reaction. *Chem. Commun.* **2013**, *49*, 4385–4387. [CrossRef] [PubMed]
38. Barrio, L.; Zhou, G.; González, I.D.; Estrella, M.; Hanson, J.; Rodriguez, J.A.; Navarro, R.M.; Fierro, J.L.G. *In Situ* Characterization of Pt Catalysts Supported on Ceria Modified TiO_2 for the WGS Reaction: Influence of Ceria Loading. *Phys. Chem. Chem. Phys.* **2012**, *14*, 2192–2202. [CrossRef] [PubMed]
39. Takenaka, S.; Shimizu, T.; Otsuka, K. Complete Removal of Carbon Monoxide in Hydrogen-Rich Gas Stream through Methanation over Supported Metal Catalysts. *Int. J. Hydrog. Energy* **2004**, *29*, 1065–1073. [CrossRef]
40. Kalamaras, C.M.; Americanou, S.; Efstathiou, A.M. "Redox" vs "Associative Formate with –OH Group Regeneration" WGS Reaction Mechanism on Pt/CeO_2: Effect of Platinum Particle Size. *J. Catal.* **2011**, *279*, 287–300. [CrossRef]
41. Pigos, J.M.; Brooks, C.J.; Jacobs, G.; Davis, B.H. Low Temperature Water-Gas Shift: Characterization of Pt-Based ZrO_2 Catalyst Promoted with Na Discovered by Combinatorial Methods. *Appl. Catal. A Gen.* **2007**, *319*, 47–57. [CrossRef]
42. Panagiotopoulou, P.; Chistodoulakis, A.; Kondarides, D.I.; Boghosian, S. Particle Size Effects on the Reducibility of Titanium Dioxide and its Relation to the Water–Gas Shift Activity of Pt/TiO_2 Catalysts. *J. Catal.* **2006**, *240*, 114–125. [CrossRef]